Supporting Information for

Measurement of Gas and Aerosol Phase Absorption Spectra across the Visible and Near-IR using Supercontinuum Photoacoustic Spectroscopy

James G. Radney and Christopher D. Zangmeister[*]

Material Measurement Laboratory, National Institute of Standards and Technology, Gaithersburg, Maryland, 20899, USA

SUPPORTING INFORMATION

The Supporting Information contains further details related to the characterization of the supercontinuum laser for photoacoustic measurements such as the beam diameter and output power density as a function of wavelength and a table containing the specific wavelengths and bandwidths used and the corresponding limits of detection. The integrated absorption coefficients of water vapor for each wavelength at 10 % RH and STP is also included. We provide plots of the absorption spectra calculated using the High Resolution Transmission 2012 (HITRAN 2012) database and the overlap of the corresponding output of the tunable wavelength and bandwidth filter. The measured and calculated absorption coefficients as a function of RH at λ = 725 nm and 820 nm is included to demonstrate the linear response of our microphone to RH. Finally, significant discussion on the determination of nigrosin's wavelength dependent refractive index is included.

Tunable wavelength and bandwidth filter output beam diameter. The $1/e^2$ beam diameter of the tunable wavelength and bandwidth filter was measured as a function of wavelength and bandwidth and is shown in Fig. S2. The beam diameter was measured using a scanning knife-

edge beam profiler (ThorLabs Omega Meter WM100).[1] The beam width of a laser beam with a Gaussian profile is

$$D_{\mathrm{beam}} = 4\pi f T_{\mathrm{r}} * 16002\ \mu\mathrm{m} \quad \text{(S1)}$$

where f is the rotation speed of the profiler drum (10 Hz) and T_{r} is the rise time from 16 % to 84 % total power. As the output of the tunable wavelength filter with variable bandwidth is not Gaussian, the measured beam diameter was corrected using

$$D_{\mathrm{Corr}} = \frac{D_{\mathrm{beam}}}{M_{\mathrm{k}}}[0.81(M_{\mathrm{k}} - 1) + 1] \quad \text{(S2)}$$

where M_{k} is square root of the times-diffraction-limit factor (M^2 = 1.1). In order to not overload the profiler sensor, the output of the tunable wavelength filter with variable bandwidth was passed through an O.D. 3 neutral density filter prior to measurement.

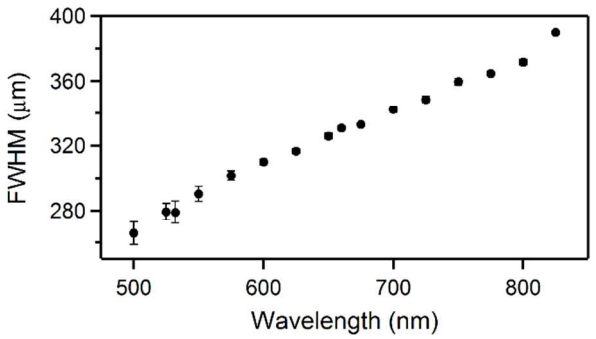

Figure S1: Output $1/e^2$ beam diameter of the tunable wavelength and bandwidth filter output as a function of wavelength for the bandwidths used presently.

Tunable wavelength and bandwidth filter output power density. The power distribution of the tunable wavelength and bandwidth filter was measured for each center wavelength longer than 600 nm using an optical spectrum analyzer (Yokogawa AQ6370C). The total power was measured at the center wavelength using a calibrated power meter. Results are shown in Fig. S2 and Table S1.

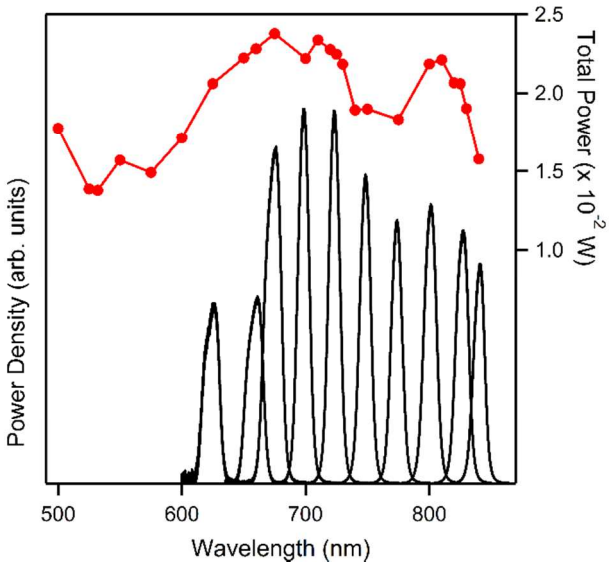

Figure S2: Output power density of the output of the tunable wavelength filter with variable bandwidth.

Table S1: Bandwidth, average peak-to-peak power, the 5 min. limit of detection and water vapor absorption coefficient at 10 % RH for each center wavelength used in the collection of aerosol absorption spectra.

Wavelength (nm)	**Bandwidth (nm)**	**Laser Power (x 10^{-2} W)**	**LOD (x 10^{-5} m^{-1})**	**α_{abs} $H_2O_{(g)}$ (x 10^{-6} m^{-1}, 10% RH)***
500	20	1.8	1.6	1.50
525	20	1.4	2.1	0.14
532	20	1.4	2.1	0.43
550	20	1.6	1.8	0.97
575	15	1.5	1.9	2.41
600	15	1.8	1.6	1.68
625	15	2.1	1.4	0.15
650	15	2.2	1.3	1.65
660	15	2.3	1.2	1.10
675	15	2.7	1.1	0.03
700	10	2.3	1.2	4.87
710	10	2.4	1.2	3.58
720	10	2.4	1.2	23.83
725	10	2.3	1.2	28.62
730	10	2.2	1.3	23.29

740	10	2.1	1.4	4.81
750	10	2.0	1.4	0.29
775	10	1.8	1.6	0.02
800	10	2.2	1.3	3.03
810	10	2.2	1.3	17.20
820	10	2.1	1.4	34.25
825	10	2.1	1.4	28.03
830	10	1.9	1.5	19.72
840	10	1.6	1.8	4.39

*nominal $H_2O_{(g)}$ mole fraction of 2.76 x 10^{-3} in 1.01325 x 10^5 Pa (1 atm)

Calculated water vapor absorption spectra. The absorption spectra of water vapor was calculated using HITRAN2012 at each wavelength used and are shown in Fig. S-3 through S-22. The corresponding laser power distributions are shown for wavelengths longer than 625 nm (the optical spectrum analyzer used presently only detects wavelengths longer than 600 nm). Atmospheric conditions at STP with a 10 % relative humidity were used. All plots have the same y-axis scale.

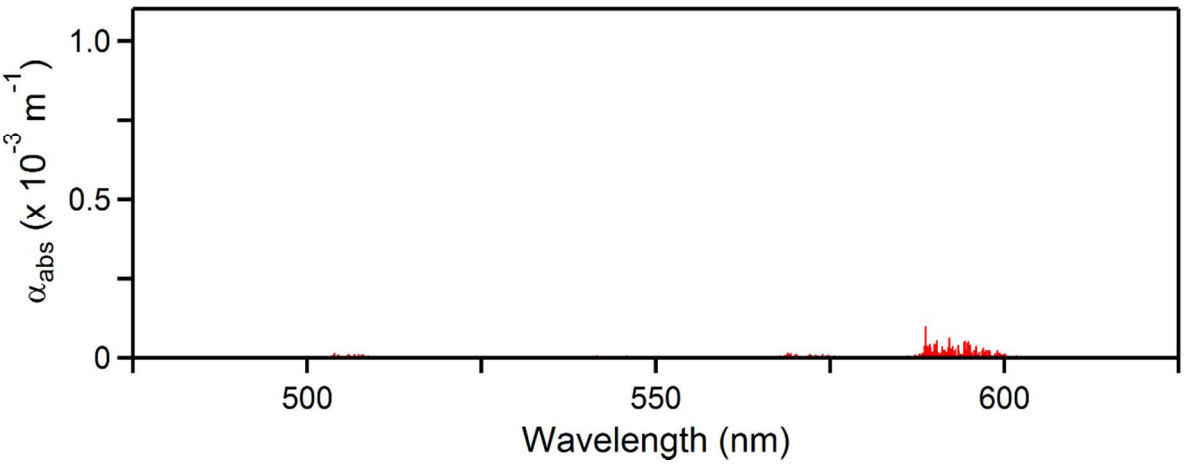

Figure S3: Calculated absorption spectrum of $H_2O_{(g)}$ from 475 nm to 625 nm laser emission band.

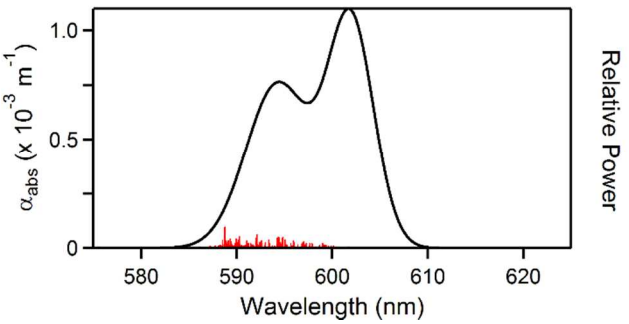

Figure S4: Calculated absorption spectrum of $H_2O_{(g)}$and measured output power distribution around the 600 nm laser emission band.

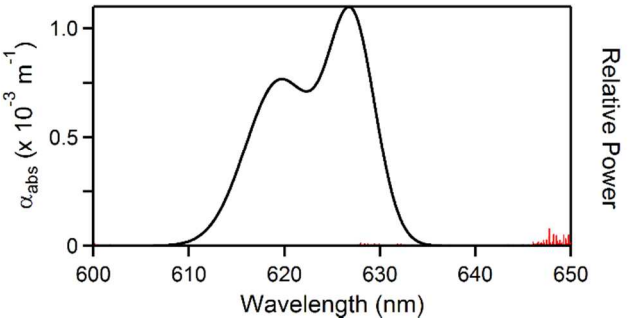

Figure S5: Calculated absorption spectrum of $H_2O_{(g)}$and measured output power distribution around the 625 nm laser emission band.

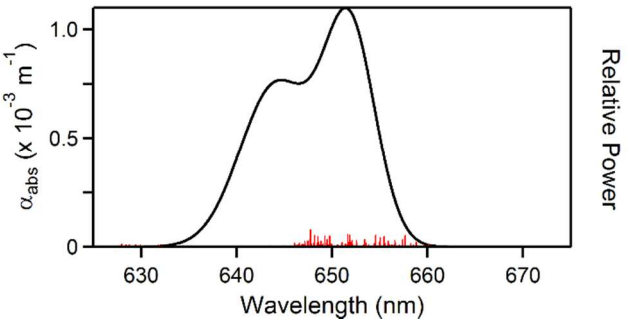

Figure S6: Calculated absorption spectrum of $H_2O_{(g)}$ and measured output power distribution around the 650 nm laser emission band.

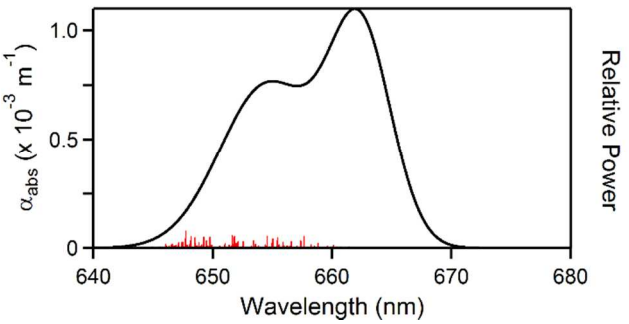

Figure S7: Calculated absorption spectrum of $H_2O_{(g)}$ and measured output power distribution around the 660 nm laser emission band.

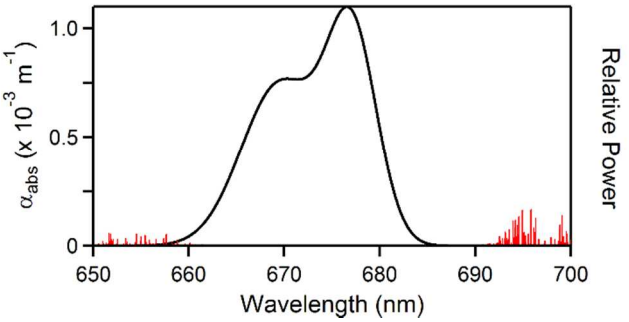

Figure S8: Calculated absorption spectrum of $H_2O_{(g)}$ and measured output power distribution around the 675 nm laser emission band.

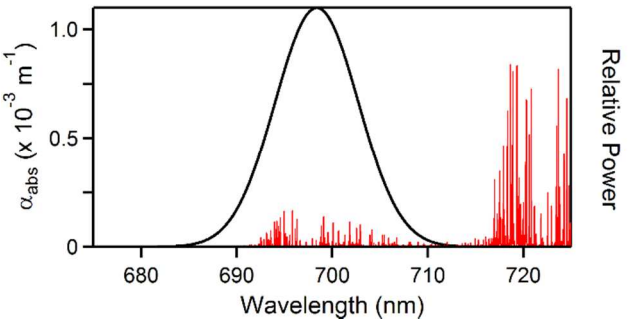

Figure S9: Calculated absorption spectrum of $H_2O_{(g)}$ and measured output power distribution around the 700 nm laser emission band.

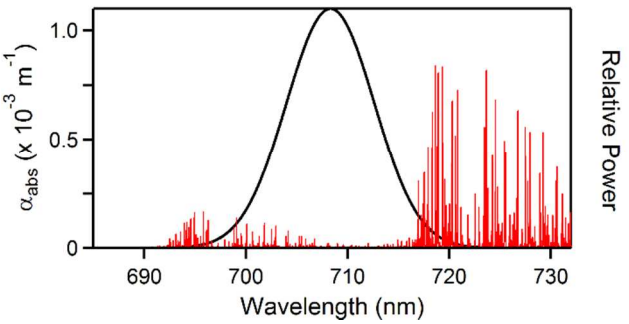

Figure S10: Calculated absorption spectrum of $H_2O_{(g)}$ and measured output power distribution around the 710 nm laser emission band.

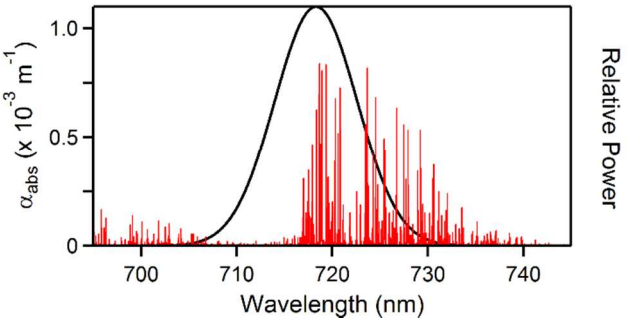

Figure S11: Calculated absorption spectrum of $H_2O_{(g)}$ and measured output power distribution around the 720 nm laser emission band.

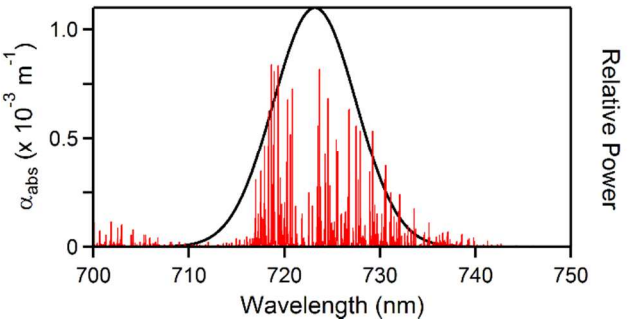

Figure S12: Calculated absorption spectrum of $H_2O_{(g)}$ and measured output power distribution around the 725 nm laser emission band.

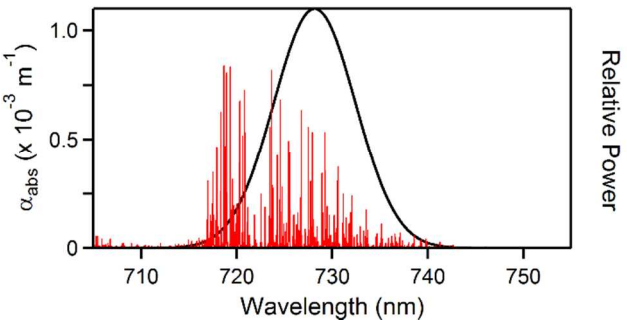

85

86 **Figure S13:** Calculated absorption spectrum of $H_2O_{(g)}$ and measured output power distribution

87 around the 730 nm laser emission band.

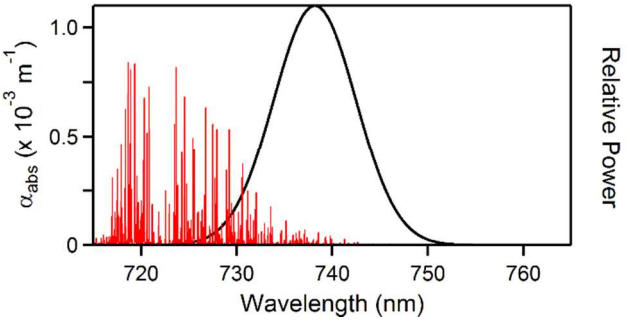

88

89 **Figure S14:** Calculated absorption spectrum of $H_2O_{(g)}$ and measured output power distribution

90 around the 740 nm laser emission band.

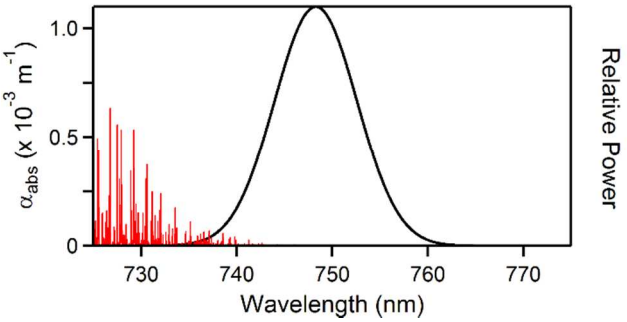

91

92 **Figure S15:** Calculated absorption spectrum of $H_2O_{(g)}$ and measured output power distribution

93 around the 750 nm laser emission band.

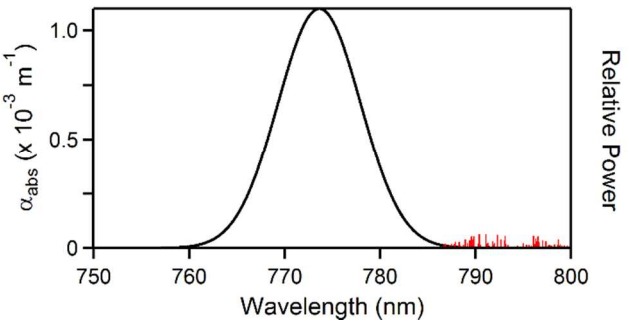

Figure S16: Calculated absorption spectrum of $H_2O_{(g)}$ and measured output power distribution around the 775 nm laser emission band.

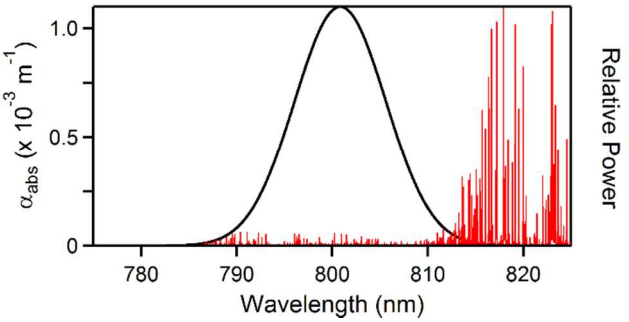

Figure S17: Calculated absorption spectrum of $H_2O_{(g)}$ and measured output power distribution around the 800 nm laser emission band.

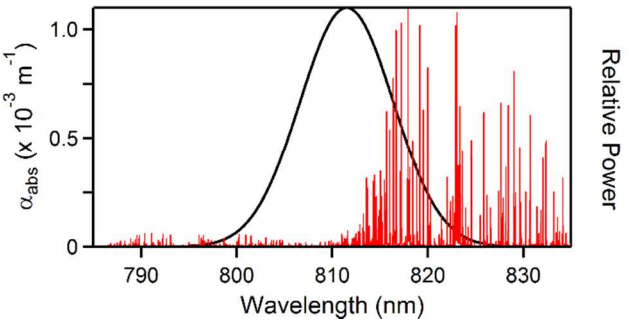

Figure S18: Calculated absorption spectrum of $H_2O_{(g)}$ and measured output power distribution around the 810 nm laser emission band.

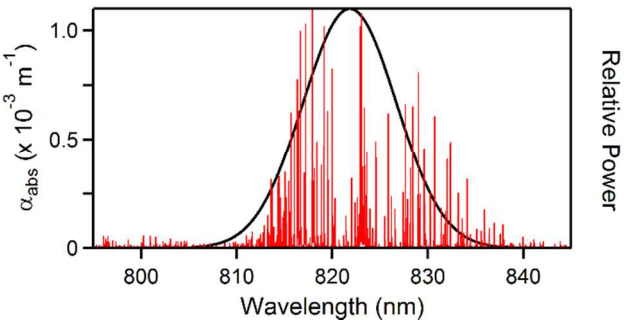

Figure S19: Calculated absorption spectrum of $H_2O_{(g)}$ and measured output power distribution around the 820 nm laser emission band.

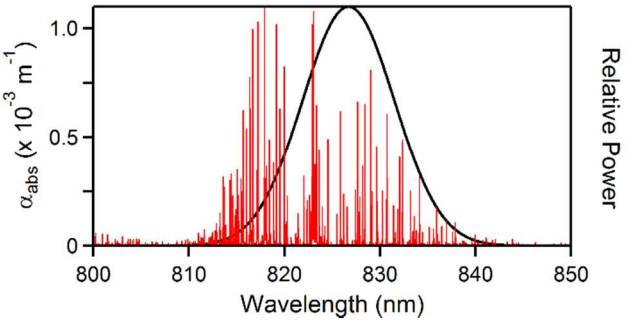

Figure S20: Calculated absorption spectrum of $H_2O_{(g)}$ and measured output power distribution around the 825 nm laser emission band.

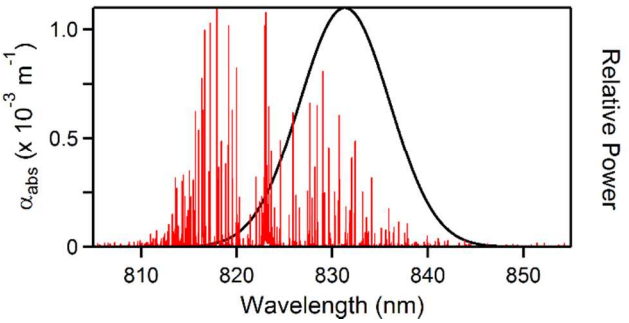

Figure S21: Calculated absorption spectrum of $H_2O_{(g)}$ and measured output power distribution around the 830 nm laser emission band.

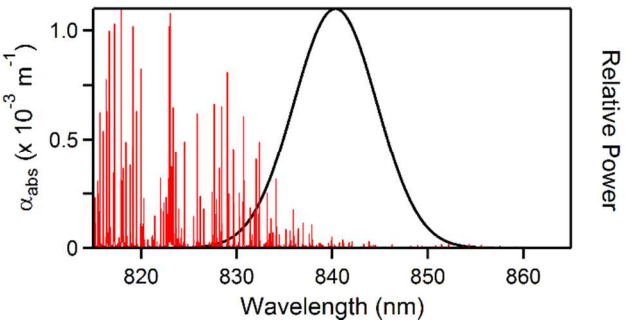

Figure S22: Calculated absorption spectrum of $H_2O_{(g)}$ and measured output power distribution around the 840 nm laser emission band.

Microphone responsivity. The response of the microphone to water vapor was measured at the peak absorption wavelengths of 725 nm and 820 nm and is shown in Fig. S23. The humidity was measured in the increasing direction on one day and then both increasing and decreasing directions on another day. Figure shows the average of those 3 scans. Error bars are 2σ. RH was allowed to stabilize for 5 min before the absorption was measured. The relative responses are 1.04 ± 0.04 and 0.97 ± 0.04 at 725 and 820 nm, respectively.

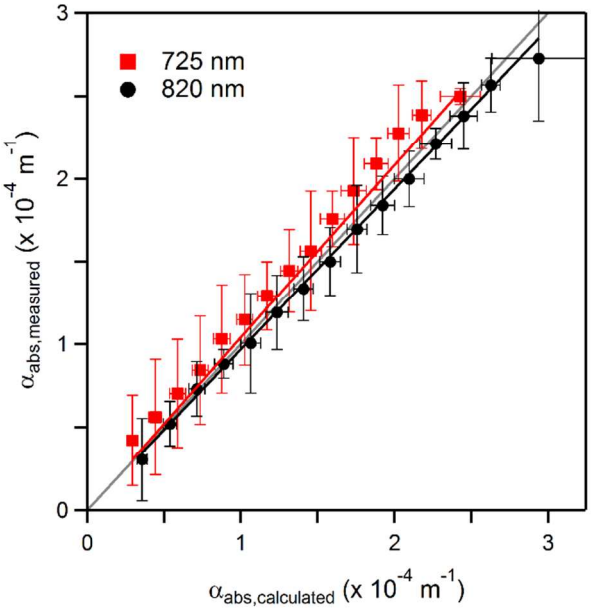

Figure S23: Microphone response as a function of RH at the peak absorption wavelengths of 725 nm and 820 nm. Grey line corresponds to 1 to 1.

Determination of Nigrosin Refractive Index. The refractive index of nigrosin aerosol at λ = 405 nm and 660 nm was determined by measuring the number concentration and extinction mass distributions at multiple particle diameters, calculating the corresponding extinction cross sections and fitting these cross sections with Mie theory. The block diagram for this experiment can be seen in Fig. S24.

Figure S24: Block diagram of the experimental setup to determine the refractive index of nigrosin.

The use of a tandem DMA, aerosol particle mass analyzer (APM), cavity ring-down spectrometer (CRD) and CPC for the isolation of a single particle charge of interest was first demonstrated in Radney et al. (2014).[2] Briefly, aerosols are selected by electrical mobility by a DMA. The voltage of the APM (Kanomax 3601) is ramped at a constant rotation speed to generate a distribution of particle masses at a given electrical mobility. The number concentration and extinction are continuously measured by a CPC and CRD, respectively, during the scan. From the measured distributions, C_{ext} as a function of mass is calculated in order to isolate the particle distribution of interest (charge of + 1) from others present (i.e. those possessing equivalent electrical mobility and charge > 1) via the slope of C_{ext} as in Radney et at (2014)[2]; see the Supporting Information for a description of the calculation. The number concentration distributions are fit using a number of Gaussian distribution functions corresponding to the number of charges present

$$N = \sum A_{\mathrm{N,q}} * \exp\left(\frac{-(m-m_{\mathrm{p,q}})^2}{2\sigma_{\mathrm{N,q}}^2}\right) \quad \text{(S3)}$$

where A_N is the peak amplitude, m_p is the average mass and σ_N is the $e^{-1/2}$ half width of the distribution. An identical equation can be derived for extinction by replacing N with α_{ext}. The subscript q denotes the number of charges on the particle. From the Gaussian fits of the distributions of concentration and extinction versus mass (Eq. 5 in manuscript), the effective density (ρ_{eff}) is calculated as

$$\rho_{\mathrm{eff}} = \frac{6m_{p,1}}{\pi D_{\mathrm{m}}^3} \quad \text{(S4)}$$

where D_m is the mobility diameter set by the DMA. The average extinction cross section is

$$C_{\mathrm{ext}} = \int \frac{\alpha_{\mathrm{ext}}}{N} = \frac{A_{\alpha_{\mathrm{ext}}}\sigma_{\alpha_{\mathrm{ext}}}}{A_{\mathrm{N}}\sigma_{\mathrm{N}}} \quad \text{(S5)}$$

The calculated C_{ext} are within 3 % to values calculated using Mie theory when using ammonium sulfate aerosol.[3] The refractive index is then calculated by minimizing the merit function χ^2 where[4]

$$\chi^2(m,k) = \sum_{i=1}^{N}\left[\frac{\left(C_{\mathrm{ext,measured}} - C_{\mathrm{ext,calculated}}(m,k)\right)_i^2}{\sigma_{\mathrm{ext},i}^2}\right] \quad \text{(S6)}$$

Here, $\sigma_{ext,i}$ represents the k = 2 uncertainty in C_{ext} at a given mobility diameter and mass combination i. From these calculations, the uncertainty (k = 2) in our refractive index was approximated from the locus of values satisfying

$$\chi^2 - \chi_{\mathrm{min}}^2 \leq \chi_{\mathrm{crit}}^2 \quad \text{(S7)}$$

at a 95% confidence interval for the given degrees of freedom where χ_{crit}^2 represents the upper-tail critical value. Particles spanning 100 nm ≤ D_m ≤ 450 nm were measured at 50 nm intervals for λ = 405 nm and 150 nm ≤ D_m ≤ 325 nm were measured at 25 nm intervals for λ = 660 nm. Extinction cross sections were calculated using a homogeneous sphere Mie routine based upon

Appendix A of Bohren and Huffman (1983),[5] with the refractive index (n = m + *i*k) treated as the fitted parameter. The best agreement was found to be for a refractive index of (1.63 ± 0.02) + (0.18 ± 0.01)*i* (χ^2_{min} = 11.48, χ^2_{crit}= 12.592, *N* = 8) and (1.70 ± 0.02) + (0.28 ± 0.01)*i* (χ^2_{min} = 22.65, χ^2_{crit}= 15.507, *N* = 9) at λ = 405 nm and 660 nm, respectively. These measured refractive indices correlate well with others found in the literature: 1.78 + 0.19*i* (λ = 360 nm)[6], 1.70 + 0.31*i* (λ = 532 nm)[7], 1.72 + 0.28*i* (λ = 532 nm)[8] and 1.7 + 0.24*i* (λ = 670 nm)[9].

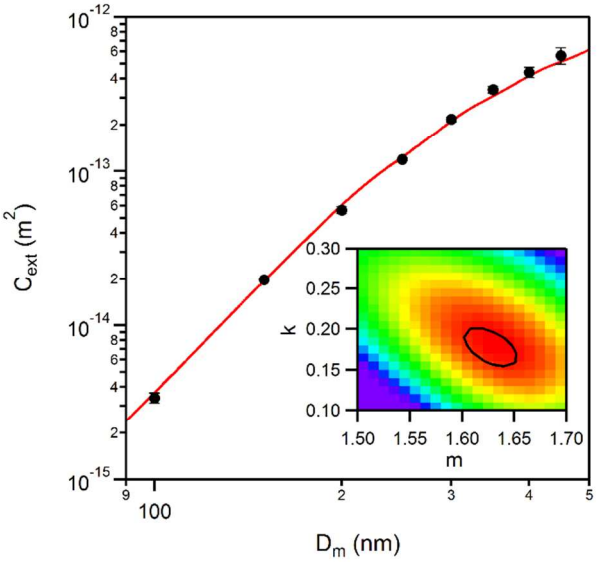

Figure S25: Fit of nigrosin refractive index at λ = 405 and n = 1.63 + 0.18*i*. Inset shows the χ^2 minimization of the data. Error bars are 2σ.

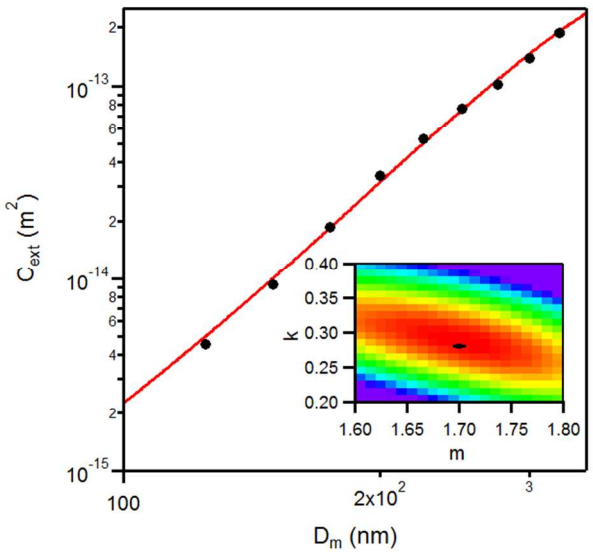

174

175 **Figure S26:** Fit of nigrosin refractive index at λ = 660 and n = 1.70 + 0.28*i*. Inset shows the χ^2

176 minimization of the data. Error bars for 2σ measurement uncertainty have been included but are

177 smaller than the corresponding data points.

178 For the real component of nigrosin's refractive index, we assumed that *m* varied linearly

179 between 405 nm and 660 nm. For wavelengths longer than 660 nm, we assumed *m* was equal to

180 1.70 (the λ = 660 nm value).

181 In order to calculate the imaginary component of the refractive index for nigrosin across the 16

182 wavelengths measured, the UV-Vis absorption spectrum of 5.0 x 10^{-3} mg mL^{-1} nigrosin solution

183 was measured under acidic (0.01 M H_2SO_4), basic (0.01 M NaOH), and neutral (DI H_2O only)

184 conditions. From the average measured aerosol effective density (1.34 g cm^{-3}) the solution MAC

185 spectrum was calculated using the Beer-Lambert law:

186 $$\mathrm{MAC} = \frac{A}{cl} \qquad \text{(S8)}$$

187 where *A*, *c* and *l* are the UV-Vis absorption, mass concentration and path length, respectively.

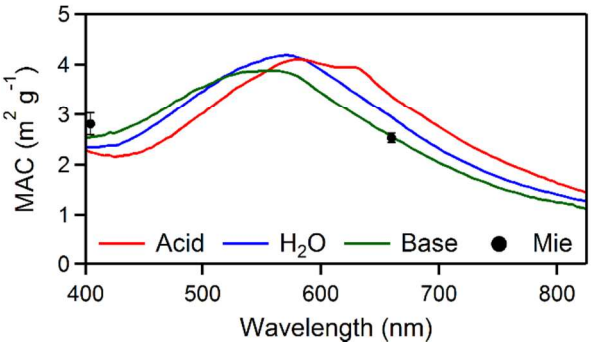

188

189 **Figure S27:** MAC spectrum of 5.0 x 10^{-3} mg mL^{-1} nigrosin solution in acidic (red), basic
190 (green) and DI H_2O (blue). Black circles correspond to the calculated solution MAC from
191 measured refractive indices at λ = 405 nm and 660 nm.

192 From the calculated refractive indices at λ = 405 nm and 660 nm, the MAC of a 1 nm particle
193 was calculated and compared to the measured UV-Vis MAC; i.e. the MAC of the 1 nm particle
194 and solution should be comparable; i.e. Rayleigh limit of particle absorption.[10] The best
195 agreement was obtained between the basic absorption spectrum and MAC. The imaginary
196 component of the refractive index was extrapolated from the basic solution spectrum assuming
197 that the nigrosin solution behaves as a bulk material, the absorption coefficient ($\alpha_{abs,bulk}$), the
198 imaginary component of the refractive index (k) and the wavelength can be related by[5]

199 $$\alpha_{\text{abs,bulk}} = \frac{4\pi k}{\lambda} \quad \text{(S9)}$$

200 Thus, it follows that

201 $$\frac{\alpha_{\lambda_1}}{\alpha_{\lambda_2}} = \frac{k_1\lambda_2}{k_2\lambda_1} = \frac{A_{\lambda_1}}{A_{\lambda_2}} \quad \text{(S10)}$$

202 The calculated imaginary component of the refractive index can be seen as the in Fig. S28.

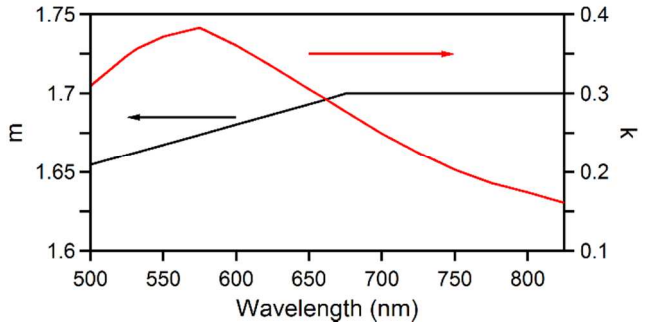

Figure S28: Calculated real (black) and imaginary (red) components of nigrosin's refractive index as a function of wavelength.

References

(1) NIST Technical Disclaimer: Certain commercial equipment, instruments, or materials (or suppliers, or software, ...) are identified in this paper to foster understanding. Such identification does not imply recommendation or endorsement by the National Institute of Standards and Technology, nor does it imply that the materials or equipment identified are necessarily the best available for the purpose.

(2) Radney, J. G.; You, R.; Ma, X.; Conny, J. M.; Zachariah, M. R.; Hodges, J. T.; Zangmeister, C. D., Dependence of Soot Optical Properties on Particle Morphology: Measurements and Model Comparisons *Environ. Sci. Technol.* **2014,** *48* (6), 3169 - 3176.

(3) Toon, O. B.; Pollack, J. B.; Khare, B. N., The Optical Constants of Several Atmospheric Aerosol Species: Ammonium Sulfate, Aluminum Oxide, and Sodium Chloride. *J. Geophys. Res.* **1976,** *81* (33), 5733-5748.

(4) Abo Riziq, A.; Erlick, C.; Dinar, E.; Rudich, Y., Optical properties of absorbing and non-absorbing aerosols retrieved by cavity ring down (CRD) spectroscopy. *Atmos. Chem. Phys.* **2007,** *7* (6), 1523-1536.

(5) Bohren, C. F.; Huffman, D. R., *Absorption and scattering of light by small particles*. Wiley: New York, 1983.

(6) Washenfelder, R. A.; Flores, J. M.; Brock, C. A.; Brown, S. S.; Rudich, Y., Broadband measurements of aerosol extinction in the ultraviolet spectral region. *Atmos. Meas. Tech.* **2013,** *6* (4), 861-877.

(7) Lack, D. A.; Lovejoy, E. R.; Baynard, T.; Pettersson, A.; Ravishankara, A. R., Aerosol Absorption Measurement using Photoacoustic Spectroscopy: Sensitivity, Calibration, and Uncertainty Developments. *Aerosol Sci. Technol.* **2006,** *40* (9), 697 - 708.

(8) Lang-Yona, N.; Rudich, Y.; Segre, E.; Dinar, E.; Abo-Riziq, A., Complex Refractive Indices of Aerosols Retrieved by Continuous Wave-Cavity Ring Down Aerosol Spectrometer. *Anal. Chem.* **2009,** *81* (5), 1762-1769.

(9) Woo, C. G.; You, S.; Lee, J., Determination of refractive index for absorbing spheres. *Optik* **2013,** *124* (21), 5254-5258.

(10) Moosmüller, H.; Arnott, W. P., *Particle optics in the Rayleigh regime*. 2009; Vol. 59, p 1028-31.

236